Effect of synthetic jet modulation schemes on the reduction of a laminar separation bubble

J. H. Seo,* F. Cadieux, and R. Mittal†
Department of Mechanical Engineering, Johns Hopkins University, Baltimore, Maryland 21218, USA

E. Deem and L. Cattafesta
Department of Mechanical Engineering, Florida State University, Tallahassee, Florida 32310, USA

(Received 30 September 2017; published 12 March 2018)

The response of a laminar separation bubble to synthetic jet forcing with various modulation schemes is investigated via direct numerical simulations. A simple sinusoidal waveform is considered as a reference case, and various amplitude modulation schemes, including the square-wave "burst" modulation, are employed in the simulations. The results indicate that burst modulation is less effective at reducing the length of the flow separation than the sinusoidal forcing primarily because burst modulation is associated with a broad spectrum of input frequencies that are higher than the target frequency for the flow control. It is found that such high-frequency forcing delays vortex roll-up and promotes vortex pairing and merging, which have an adverse effect on reducing the separation bubble length. A commonly used amplitude modulation scheme is also found to have reduced effectiveness due to its spectral content. A new amplitude modulation scheme which is tailored to impart more energy at the target frequency is proposed and shown to be more effective than the other modulation schemes. Experimental measurements confirm that modulation schemes can be preserved through the actuator and used to enhance the energy content at the target modulation frequency. The present study therefore suggests that the effectiveness of synthetic jet-based flow control could be improved by carefully designing the spectral content of the modulation scheme.

DOI: 10.1103/PhysRevFluids.3.033901

I. INTRODUCTION

Over the last two decades, zero-net mass-flux (ZNMF) jets (also called "synthetic jets") have proved to be effective tools for separation control on low to moderate Reynolds number airfoils. Experimental studies have examined the effective actuator designs and nondimensional frequencies for separation control, and have provided insights into the process by which the synthetic jet affects the separated shear layer and separation length [1–5]. Simulations have enabled a better understanding of the dynamics of synthetic jets, the response of the flow from the perspective of hydrodynamic stability, and the phenomenon of lock-on observed between the frequencies of the shear layer, separated shear layer, and the wake [6–14]. In experiments, the jet (or carrier) frequency is generally chosen to be close to one of the natural frequencies of the actuator to increase output. Since this frequency can be orders of magnitude higher than the frequencies effective for separation control, modulation of the carrier waveform by a low frequency waveform, either via a square wave or sine wave corresponding to burst or amplitude modulation, respectively [15], is often used to generate the desired low frequency input

*jhseo@jhu.edu
†mittal@jhu.edu

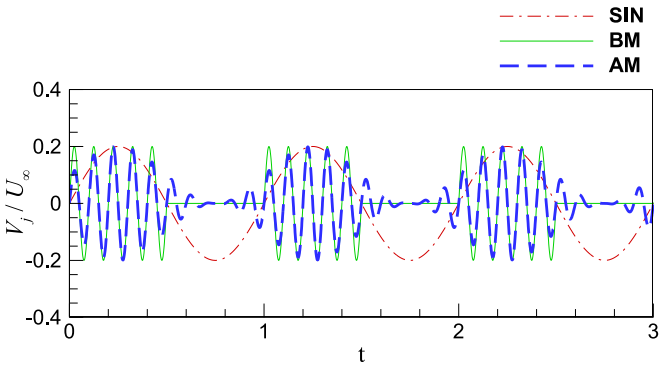

FIG. 1. Synthetic jet profiles. SIN: sinusoidal actuation [Eq. (2)]; BM: burst modulation with $f_m = 1$, $f_c = 10$, $N = 10$, and DC = 50% [Eq. (3)]; AM: sinusoidal amplitude modulation with $f_m = 1$ and $f_c = 10$ [Eq. (4)].

via nonlinear interaction. This modulation frequency is generally set such that an integer multiple N periods of the carrier signal occur within one period of the modulated signal, i.e., $1/f_m = N/f_c$ where f_c is the carrier frequency of the actuator and f_m is the modulated frequency for the flow control. The duty cycle (DC) corresponds to the fraction of time during which the actuator is powered on over one period of the modulation signal. Amplitude modulation is also sometimes employed to avoid abrupt on/off control and provide a smoother waveform [16,17]. Examples of these synthetic jet waveforms are shown in Fig. 1.

While the overall control effectiveness of various modulation schemes has been examined in past studies [15], the effect of the synthetic jet modulation on the flow-physics associated with separation control remains relatively unexplored. In most simulation-based studies, owing to the additional computational cost of resolving the high actuator frequency, only the modulated signal at target flow control frequency, f_m, is modeled, often with a simple sinusoidal time-varying signal [12,13]. Although this has proved to be a useful approximation, it is not precisely equivalent in either the jet momentum flux or in the dynamical response of the flow. This likely contributes to some of the discrepancies in control effectiveness often observed between experiments and simulations, where the baseline uncontrolled flows otherwise agree well.

In the present study, to understand these differences and to guide efforts for designing more effective synthetic jet modulation schemes, the effects of synthetic jet modulation on the response of separation bubble are investigated using direct numerical simulations of a laminar separation bubble flow over a flat plate. Simulations with a variety of jet amplitude modulation schemes are carried out, and the effectiveness of each modulation scheme examined vis-à-vis the flow physics of the forced separation bubble. The culmination of these simulations is the analysis of a new modulation scheme that is demonstrated to be more effective for the control of separation. Preliminary benchtop tests with a zero-net mass flux actuator are used to examine the realizability and actuator efficiency of this newly proposed scheme.

II. METHOD

The separated flow configuration is modeled after recent experiments of separation control over an elliptical leading-edge flat plate with zero-net suction and blowing from the top of the wind tunnel to induce a transitional separation bubble [15,18]. The present simulations focus on the region near the trailing edge of the flat plate where the flow separation and reattachment occur, including a few boundary layer thicknesses upstream where the ZNMF synthetic jet slot is located. Figure 2 shows the schematic of the simulation setup. The inflow condition is corresponding to a $\mathrm{Re}_x = 66\,000$ in the experiment and a matching Blasius inflow with the appropriate boundary layer thickness is

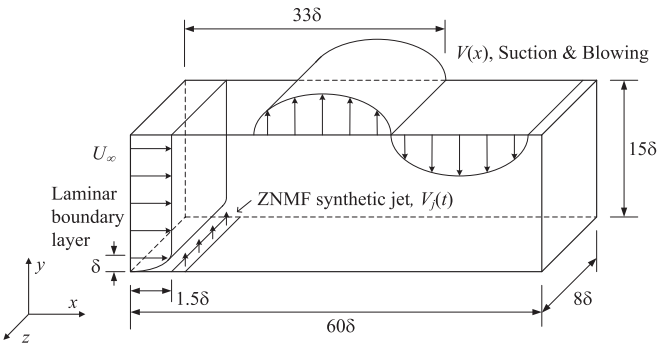

FIG. 2. Schematic of a simulation setup.

applied. Lengths are henceforth nondimensionalized by the inlet boundary layer thickness, δ. The flow Reynolds number based on the inflow boundary layer thickness (δ) is $\mathrm{Re}_\delta = 1000$. The domain size is 60δ in the streamwise direction (x) and 15δ in the vertical direction (y). The spanwise domain size is set to 8δ and a periodic boundary condition is applied in this direction (z). The adequacy of this spanwise domain size is assessed in Appendix B. Similarly to the experiment, a sinusoidal suction and blowing profile is applied on the top boundary to generate flow separation and reattachment, and the vertical velocity profile for the suction and blowing is given by [19]

$$V(x) = -V_s \sin(2\pi(x - x_s)/L_s) \exp\{-a_s(2(x - x_s)/L_s)^{b_s}\}, \tag{1}$$

where the following parameters are used: $V_s = 0.5U_\infty$, $x_s = 33\delta$, $L_s = 50\delta$, $a_s = 10$, and $b_s = 20$. The streamwise velocity at the ceiling of the domain is determined using a no-vorticity boundary condition. The ZNMF synthetic jet is modeled using a simple slot where vertical velocity is imposed at the wall between $x = 1.5\delta$ and $x = 2\delta$ as shown in Fig. 2. The temporal profile of synthetic jet velocity is given by

$$V_{j,\mathrm{SIN}}(t) = V_{\max} \sin(2\pi f_m t) \tag{2}$$

for the sinusoidal jet and

$$V_{j,\mathrm{BM}}(t) = V_{\max} \sin(2\pi f_c t) 0.5[1 + \mathrm{sgn}\{\sin(2\pi f_m t + \phi) - \sin(\phi)\}] \tag{3}$$

for the burst modulation (BM) scheme, where $\phi = \{1 - 2(\mathrm{DC}/100)\}\pi/2$ and DC (%) is the duty cycle. The commonly used amplitude modulation scheme [17], where the amplitude is modulated using a sinusoidal function, is given by

$$V_{j,\mathrm{AM1}}(t) = \left(\frac{1}{2}\right) V_{\max} \sin(2\pi f_c t)\{1 + \sin(2\pi f_m t)\}, \tag{4}$$

and is also examined in the current study. Over the synthetic jet outlet ($1.5\delta \leqslant x \leqslant 2\delta$), the vertical velocity (v) is spatially uniform and set to the jet velocity, V_j. The streamwise velocity (u) at the outlet of the synthetic jet is set to zero during the expulsion process ($u = 0$ for $V_j > 0$), but a Neumann condition is imposed during the ingestion phase ($du/dy = 0$ for $V_j < 0$) to ensure a more realistic velocity distribution near the jet exit [12].

Simulations are performed by solving the incompressible Navier-Stokes equations:

$$\nabla \cdot \vec{u} = 0, \quad \frac{\partial \vec{u}}{\partial t} + (\vec{u} \cdot \nabla)\vec{u} + \frac{\nabla p}{\rho} = \nu \nabla^2 \vec{u}, \tag{5}$$

where $\vec{u} = (u, v, w)$ is the flow velocity vector, p is the pressure, ρ and ν are the density and kinematic viscosity of the fluid, respectively. The equations are solved by using an in-house three-dimensional (3D) Cartesian immersed boundary solver, VICAR3D [20]. The solver has second-order accuracy in space and time and allows for both direct numerical simulations and large-eddy simulations. In this study, direct numerical simulations are conducted with a resolution of $512 \times 128 \times 32$ in the streamwise, wall-normal, and spanwise directions, respectively. The mesh in the streamwise direction is nonuniform and employs 12 points across the synthetic jet exit. The vertical grids are stretched to cluster points inside the boundary layer where the minimum grid spacing is 0.02δ. This resolution is chosen based on the grid refinement study presented in the Appendix A. Given that the laminar separation bubble undergoes transition, the grid spacing in terms of wall units is also provided: the average and maximum grid spacings in the stream and spanwise directions are found to be $\Delta x^+_{,\text{avg}} = 3.9$, $\Delta x^+_{,\text{max}} = 15.6$ and $\Delta z^+_{,\text{avg}} = 6.2$, $\Delta z^+_{,\text{max}} = 20.8$, and for the first grid spacing in the wall normal direction the values are $\Delta y^+_{1,\text{avg}} = 0.25$, and $\Delta y^+_{1,\text{max}} = 0.8$. These values are within the typical range for accurate direct numerical simulation of transitional wall-bounded flows. The flow simulations have performed on the MARCC (Maryland Advanced Research Computing Center) cluster using 64 CPU cores, and the simulation for nondimensional time, $2000\delta/U_\infty$, took about 32 hours for the baseline flow with no control, and 40–50 hours for the control cases depending on modulation schemes.

III. RESULTS AND DISCUSSION

A. Baseline separated flow

A simulation of the baseline separated flow with no control is performed and the flow structure at one time instance is shown in Fig. 3(a). The plot shows how the laminar boundary layer separates due to the adverse pressure gradient induced by the steady suction and blowing from the top of the domain, rolls up, and starts shedding spanwise rollers that quickly experience a secondary spanwise instability and breakdown into a turbulent flow near the reattachment location.

The time averaged skin friction coefficient $C_f = \tau_w/(0.5\rho U_\infty^2)$ and the pressure coefficient $C_p = (p - p_\infty)/(0.5\rho U_\infty^2)$ are examined in Fig. 3(b) to find the mean separation bubble length. The flow field is averaged in time for $2000\delta/U_\infty$, which corresponds to about 120 vortex shedding cycles. The flow in the separation region is laminar and nearly periodic, and thus the separation point can easily be determined by the first zero-crossing of the C_f, in the vicinity of the expected separation point. The flow in the reattachment region is, however, turbulent and highly unsteady with a wide range of spatial and temporal scales. This results in multiple zero-crossings of the C_f in the separated zone, making it difficult to determine the reattachment point based on the skin friction, especially when the time interval used for averaging is not long enough. Based on the fact that the wall pressure rises at the reattachment region [21], we define the reattachment point as the location of peak C_p. This criteria was employed in our previous study [22] to assess time-dependent changes in the length of the separation bubble with a short-term time averaging (for 1–2 vortex shedding cycles), because it is less sensitive to the length of time interval and provides a robust estimation of the separation length. In the present study, we use the same criteria for the long-term time averaged flow (for about 120 vortex shedding cycles) for consistency with the previous study. This definition is also deemed adequate for the purpose of comparison herein. The mean separation bubble length L_{sep} is defined by the distance between the separation and reattachment points as shown in Fig. 3(b). For the baseline flow, the separation point is located at $x/\delta = 7.6$ and the L_{sep} is found to be about 42.4δ.

The height of the separation bubble may be defined by the maximum displacement thickness (δ^*) along the streamwise direction. The displacement thickness is calculated by

$$\delta^* = \int_0^{y_1} \left(1 - \frac{u}{U_\infty}\right) dy. \tag{6}$$

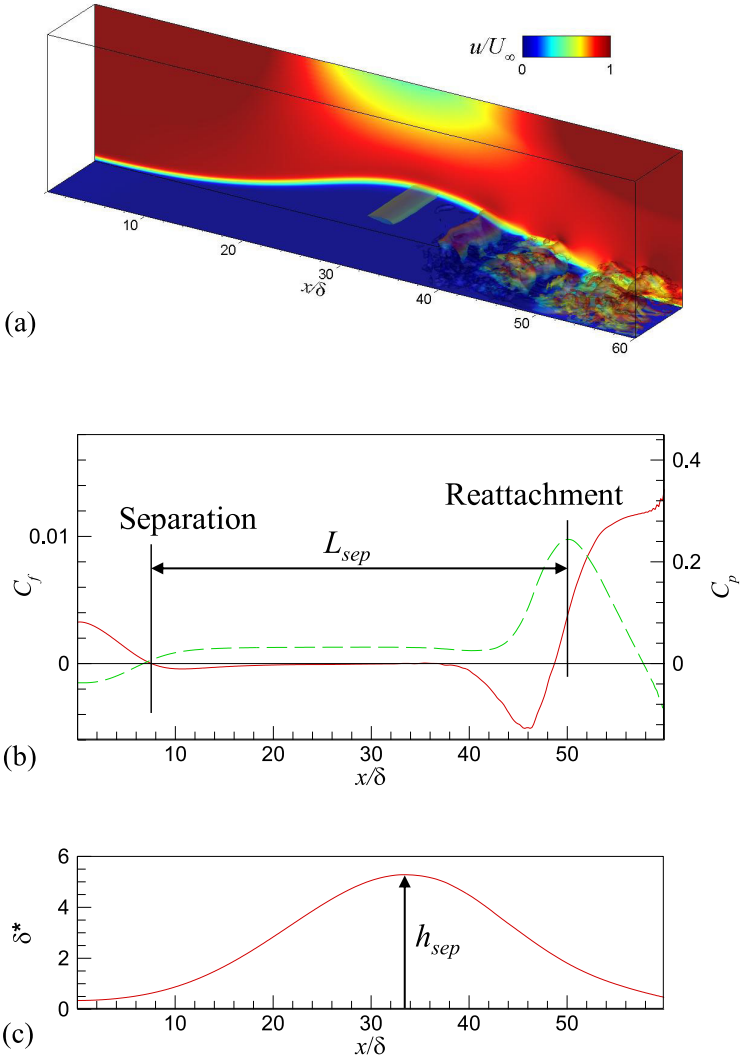

FIG. 3. (a) Instantaneous vortical structure visualized by the isosurface of the second invariant of velocity gradients (Q_2) for the baseline (no control) case. The color contour represents the streamwise velocity. (b) Time averaged skin friction (C_f, solid line) and pressure (C_p, dashed line) coefficient profiles. The separation location is determined by the first zero-crossing of C_f, and the reattachment point is identified by the peak C_p location. L_{sep} represents the mean separation bubble length. (c) Mean displacement thickness along the streamwise direction. The separation bubble height (h_{sep}) is defined by the maximum displacement thickness.

The integration in the wall normal direction (y) is performed only up to $y_1 = 6\delta$ to exclude the effect of the suction and blowing on the top boundary. The profile of displacement thickness for the mean flow is plotted in Fig. 3(c), and the separation bubble height (h_{sep}) is about 5.3δ for the baseline flow.

The instantaneous flow field [Fig. 3(a)] exhibits the roll-up and shedding of spanwise rollers. The energy spectra of the velocity fluctuations at the streamwise locations, $x/\delta = 40$ and 50, are plotted in Fig. 4, where the velocities are monitored at a distance of 2δ above from the wall. The spectra are broadband, but a discrete peak is observed at the Strouhal number, $\text{St} = f_0\delta/U_\infty = 0.06$, which corresponds to the dominant vortex shedding frequency of the separation bubble. The shedding

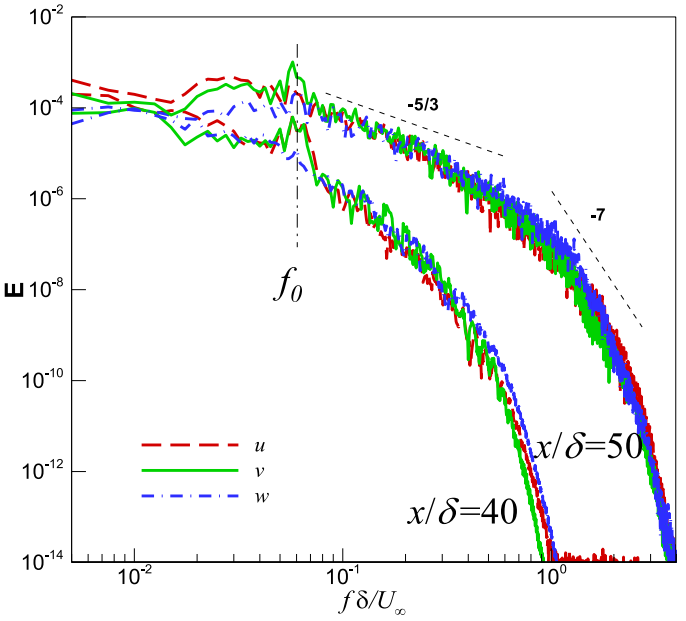

FIG. 4. Velocity spectra at $x/\delta = 40$ and 50, located 2δ above from the wall for the baseline case. A discrete peak associated with the vortex shedding in the bubble is observed and is identified as f_0.

frequency nondimensionalized by the mean separation bubble length (L_{sep}) is $St_{Lsep} = f_0 L_{sep}/U_\infty = 2.54$, and this matches well with the experimental measurement ($St_{Lsep} = 2.51$) [18]. This dominant unstable frequency, f_0, is therefore, used as a baseline forcing frequency for the separation bubble control. Note that at $x/\delta = 50$ the flow becomes turbulent, and the spectral energy decaying slopes corresponding to a narrow inertial ($-5/3$) and dissipation (-7) ranges are observed in the spectrum.

B. Separation control using ZNMF jet forcing

Simulations of the separation control using the ZNMF synthetic jet are performed for the ideal, sinusoidal (SIN) jet and the burst modulation (BM) jet. A nondimensional frequency $F^+ = f/f_0$ is introduced to characterize the forcing frequency of the synthetic jet. For the sinusoidal jet, the forcing frequency is set to $F_m^+ = f_m/f_0 = 1$, and the burst modulation used the following parameters: $F_c^+ = 10$, $F_m^+ = f_m/f_0 = 1$, and DC = 50%. For both cases, the synthetic jet amplitude, V_{max}, is set to $0.2U_\infty$. The synthetic jet profiles for these cases are shown in Fig. 1 (SIN and BM).

The contours for the time averaged streamwise velocity for the SIN and BM jet forcing are shown in Figs. 5(a) and 5(b), and the figures clearly show the effect of the synthetic jet on the average separation bubble size. The SIN jet forcing with the actuation frequency matched to the dominant unstable frequency of the separation bubble ($F_m^+ = 1$) is very effective at reducing the separation bubble size. As shown in Fig. 5(c), the mean separation bubble length is significantly reduced from 42.4δ to 28δ with the SIN jet control. The separation is delayed until $x/\delta = 9.6$, and the reattachment point also moves upstream to about $x/\delta = 38$. Note that the height of the separation bubble is also significantly reduced from 5.3δ to 3.26δ with the SIN jet control. The BM jet with the modulation frequency matched to the unstable frequency ($F_m^+ = 1$) also reduces the mean separation bubble length to 32δ [Fig. 5(d)], but not to the same degree as the SIN jet control. The separation point moves slightly downstream ($x/\delta = 8$) compared to the baseline case, and the mean reattachment point moves to approximately $x/\delta = 40$. The separation bubble height for the BM jet is $h_{sep} = 4.04\delta$ [Fig. 5(f)], which is also higher than the SIN jet case. However, since DC = 50%, the net momentum flux of the BM jet is 50% of the SIN jet, the degraded effectiveness of BM cannot, without further

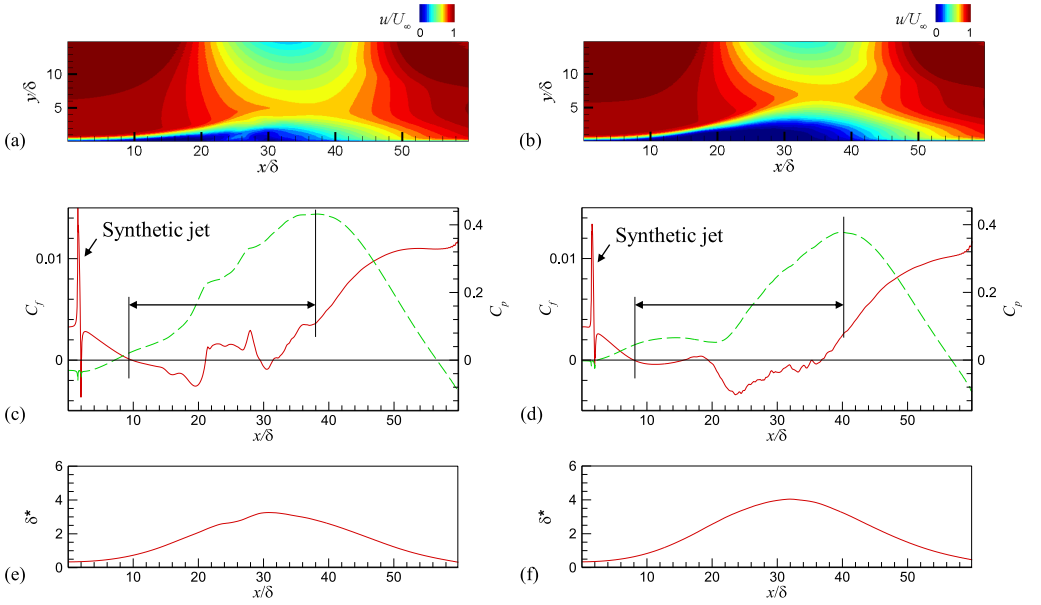

FIG. 5. Time averaged fields for the control cases with the ZNMF synthetic jet. Streamwise velocity contours for the sinusoidal jet case with $F_m^+ = 1$ (a), and the burst modulation jet with $F_c^+ = 10$, $F_m^+ = 1$, and DC = 50% (b). Skin friction (solid line) and pressure (dashed line) coefficient profiles for the sinusoidal jet (c) and the burst modulation jet (d). Mean displacement thickness along the streamwise direction for the sinusoidal jet (e) and the burst modulation jet (f).

analysis, be attributed to the nature of the modulation scheme. This will be discussed further in Sec. III C.

The instantaneous flow fields for the SIN and BM jet controls are shown in Fig. 6, and are quite different for these two cases. For the SIN jet control, the shear layer of the separation bubble initially

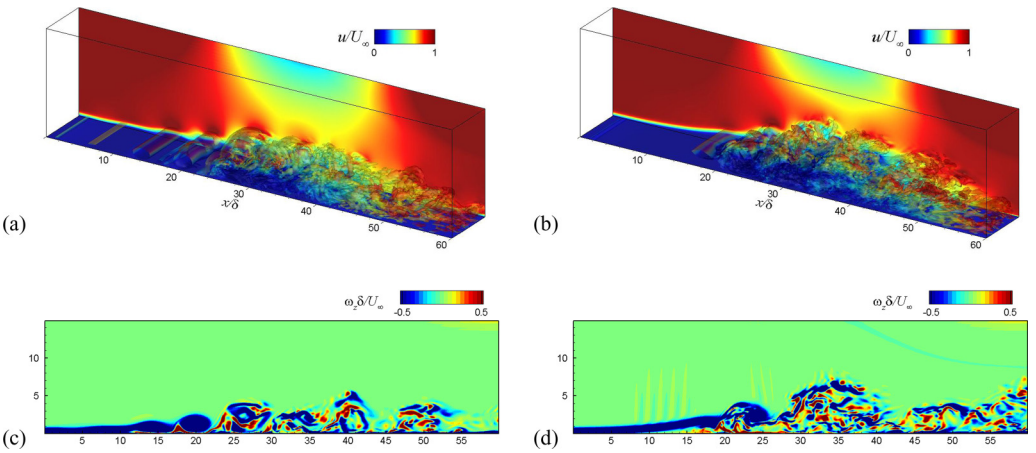

FIG. 6. Instantaneous flow fields for the control cases with the ZNMF synthetic jet. 3D vortical structure visualized by the isosurface of the second invariant of the velocity gradient (Q_2) for the sinusoidal (SIN) jet case with $F_m^+ = 1$ (a), and the burst modulation (BM) jet with $F_c^+ = 10$, $F_m^+ = 1$, and DC = 50% (b). Spanwise vorticity (ω_z) contours for the SIN jet (c) and the BM jet (d).

TABLE I. Effect of burst modulation parameters on the separation bubble control.

Case	F_m^+	F_c^+	DC (%)	C_μ	L_{sep} (δ)	h_{sep} (δ)
No control					42.4	5.3
a	1	10	50	0.01	32	4.04
b	1	20	50	0.01	33	4.42
c	1	10	50	0.02	31	4.04
d	1	10	20	0.02	32	4.13
e	1	10	10	0.002	34	4.35

rolls into vortices. This forms a two-dimensional vortex street in the upstream region [Fig. 6(a)], which breaks into smaller eddies leading to transition at around $x = 25\delta$ [Fig. 6(c)]. Note that individual packets of vorticity are clearly visible in the SIN jet control case. In the BM jet case, on the other hand, it is observed that the vortices in the separation bubble merge into large coherent vortex structures before breaking into smaller eddies [Figs. 6(b) and 6(d)]. For the BM jet, the flow transitions to turbulence earlier in space and becomes fully three-dimensional in nature immediately downstream of $x = 20\delta$. It is also interesting to note that, for the BM case, the shear layer at the upstream region ($x/\delta \sim 10$–15) is clearly detached from the wall [Fig. 6(d)], while it remains close to the wall for the SIN case [Fig. 6(c)]. In fact, the two-dimensional vortex roll-up of the upstream ($x/\delta < 20$) shear layer starts earlier for the SIN case from around $x/\delta \sim 10$, but it is delayed till $x/\delta \sim 15$ for the BM case. In addition to this, the downstream vortex merging may result in a larger mean separation bubble size than the SIN jet control case. These observations suggest that the degraded effectiveness of the BM jet on the separation bubble control might be at least partially related to the unique flow characteristics associated with the burst modulation.

C. Effect of modulation parameters

It has been shown that the effectiveness of the ZNMF jet for separation control depends on the ratio of jet momentum flux to the base flow momentum flux [15]. In this study, since the synthetic jet area and the cross sectional area of the base flow do not change, the momentum coefficient is simply defined by

$$C_\mu = \frac{(V_{j,\text{RMS}})^2}{{U_\infty}^2}, \tag{7}$$

where $V_{j,\text{RMS}}$ is the root-mean-squared value of the synthetic jet velocity calculated by

$$(V_{j,\text{RMS}})^2 = \frac{1}{T}\int_0^T V_j(t)^2 dt, \tag{8}$$

and $T = 1/f_m$. As mentioned in the previous section, in order to compare the control effectiveness for the various modulation schemes, the momentum coefficients should be matched. The BM scheme involves a number of parameters such as the modulation and carrier frequencies (f_m and f_c), duty cycle (DC), and jet amplitude (V_{max}). For the BM, the jet momentum flux depends on both DC as well as V_{max}. In this section, simulations are performed for the BM jet control with various parameters to investigate their effect on separation control. The parameters for the various cases are summarized in Table I and the corresponding synthetic jet profiles are plotted in Fig. 7. Table I also shows the momentum coefficient for each case, and the resulting mean separation bubble length (L_{sep}) and height (h_{sep}). In keeping with past practice for such investigations [13,19], the separation bubble length L_{sep} is chosen as the primary metric for representing the effectiveness of control.

Although not shown here, it is observed that the flow fields for all BM cases are very similar to the ones shown in Figs. 6(b) and 6(d), but the mean separation bubble sizes are slightly different for the parameters as listed in Table I. The results presented in Table I are also plotted in Fig. 8, and

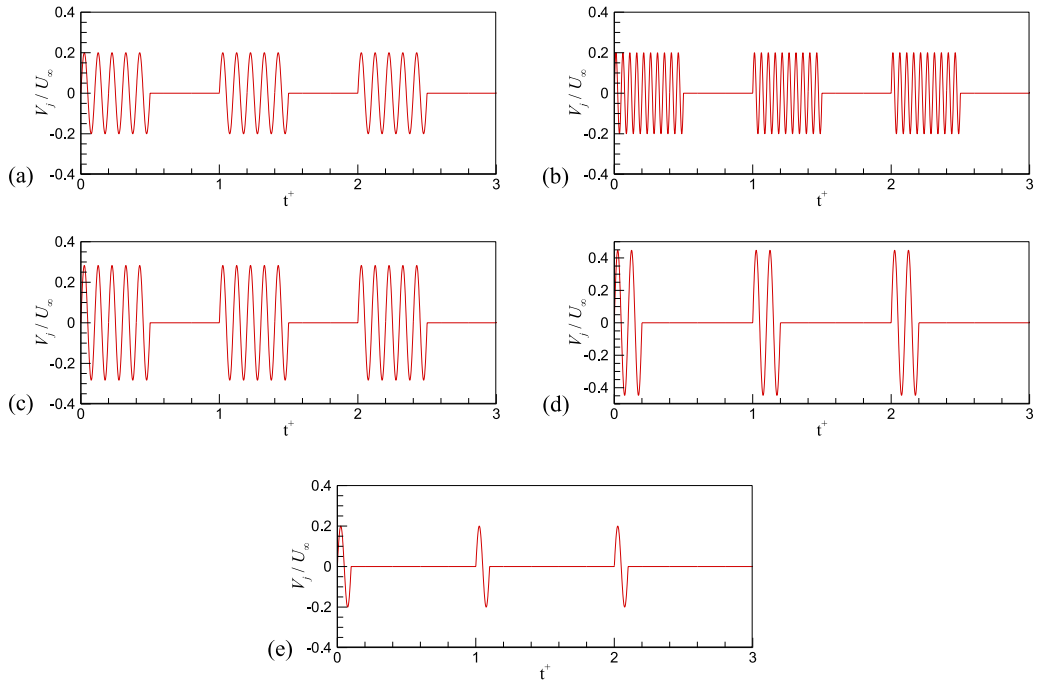

FIG. 7. Synthetic jet profiles for the burst modulation cases listed in Table I (a)–(e).

this provides a convenient view of the overall trend. For comparison, an additional simulation for the SIN jet control case with $C_\mu = 0.01$ is performed and marked in Fig. 8. In general, a larger C_μ results in a shorter separation length, i.e., more effective separation control. Note, however, that even with the same C_μ value, the BM jet is noticeably less effective than the SIN jet. This result confirms the notion that the degraded control effectiveness of the BM jet is mainly due to the altered flow characteristics, as discussed in Sec. III B.

D. Effect of forcing frequency

The BM is designed to generate a forcing at the low frequency of f_m via modulation of the high frequency f_c at which the synthetic jet is generated by the actuator. In order to assess the effectiveness of the BM to generate the modulation frequency f_m, the spectrum of the input velocity signal corresponding to the BM jet [Eq. (3)] used in Sec. III B is shown in Fig. 9(a). The spectrum of the input wave signal for the sinusoidal jet is also plotted in the figure for comparison. As expected, the spectrum of the SIN jet shows a single peak at $F^+ = 1$, while the BM jet exhibits many discrete peaks with a dominant peak located at the carrier frequency ($F^+ = 10$). A discrete peak at the modulation frequency ($F^+ = 1$) is also visible for the BM jet, but it is noted that the spectral peak at $F^+ = 1$ is about one order of magnitude smaller than the peak at $F^+ = 10$ and, furthermore, the energy content of some higher harmonics ($F^+ = 3,5,7, \ldots$) is larger than the one at $F^+ = 1$.

As discussed in the previous study of Raju *et al.* [23], the momentum forcing by the actual ZNMF synthetic jet actuator includes the nonlinear effect associated with minor pressure loss due to exit (or entrance) flow through the actuator slot. The analysis is summarized in Appendix C, and it shows that the nonlinear term can introduce additional frequency components via the action of the nonlinearity. Although the present simulations do not include the model of the actuator slot, the frequency components caused by the nonlinear effect can be observed by monitoring the jet velocity in the flow field near the synthetic jet outlet as shown in Appendix C. The synthetic jet velocities interacting with the base flow are monitored at the center of the synthetic jet outlet port, half a grid

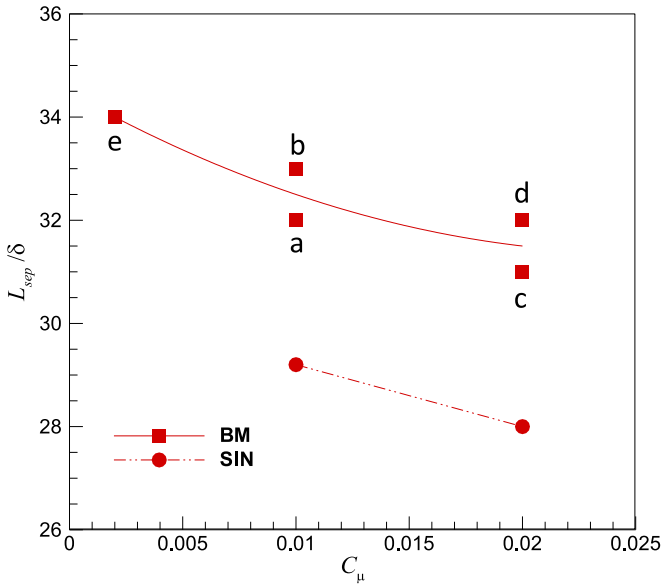

FIG. 8. Mean separation bubble length (L_{sep}) versus the momentum ratio coefficient (C_μ). (a)–(e) BM jet controls listed in Table I. SIN: sinusoidal jet control case shown for the comparison. The solid line represents the quadratic best fit for the BM cases.

spacing above the wall location ($y = \Delta y_{\text{min}}/2$) for both BM and SIN cases, and the power spectra of the monitored vertical velocity (v) are plotted in Fig. 9(b). For a fair comparison, the spectral energy is normalized by the RMS of input velocity, $(V_{j,\text{RMS}})^2$ [Eq. (8)]. Due to the nonlinear effects in the flow field, the spectrum of the SIN jet shows additional peaks at the harmonics, but the energy at $F^+ = 1$ is the most dominant and is about three orders of magnitude higher than the one at $F^+ = 2$. The analysis in Appendix C shows that, for the present flow conditions, even including the flow through the actuator slot, the magnitude of the nonlinear effect is estimated to be about 10% of the

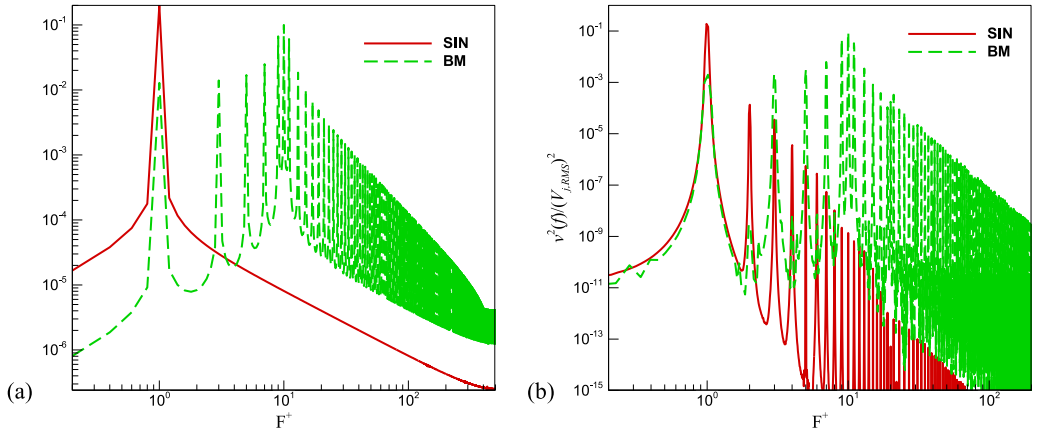

FIG. 9. (a) Frequency spectra of the synthetic jet velocity input signal. (b) Power spectra of vertical velocity monitored on the synthetic jet outlet port in the flow field. The spectral energy is normalized by the RMS of synthetic jet input velocity. SIN: sinusoidal jet at $F_m^+ = 1$; BM: burst modulated jet with $F_c^+ = 10$, $F_m^+ = 1$, and DC = 50%.

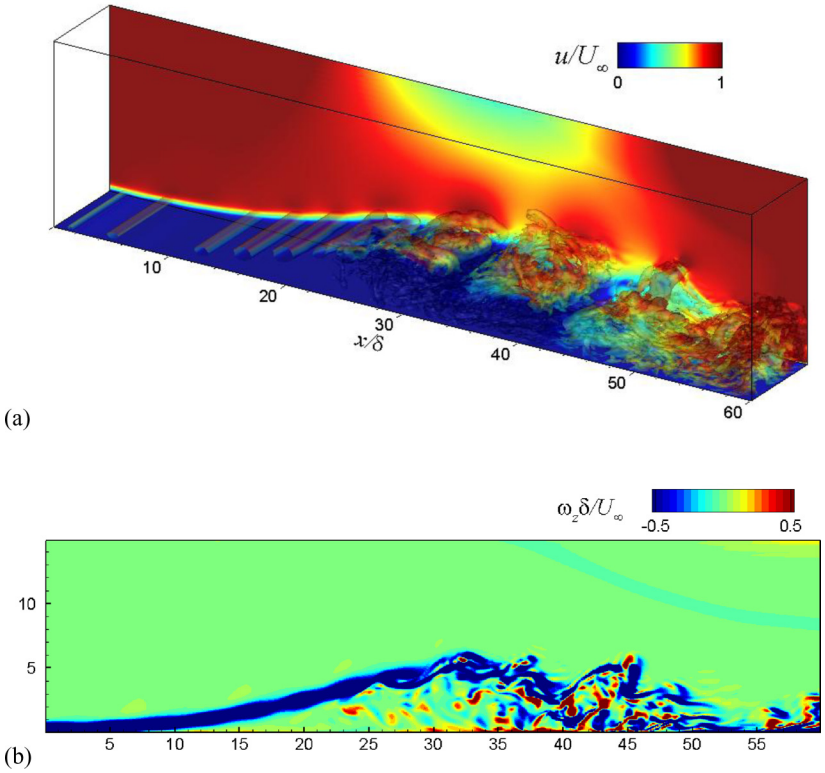

FIG. 10. Instantaneous flow fields for the sinusoidal jet control at $F^+ = 2$. (a) Vortex structures visualized by the isosurface of the second invariant of velocity gradients (Q_2). (b) Spanwise vorticity (ω_z) contours.

unsteady term. For the BM jet, even with the nonlinear effect included, the energy at higher odd harmonics is still larger than the one at $F^+ = 1$, and the normalized energy at $F^+ = 1$ is about two orders of magnitude smaller than the one for the SIN jet. This observation indicates that the forcing with the BM jet may be significantly affected by frequencies that are higher than the modulation frequency ($F^+ > 1$).

Based on the computational results presented in the previous sections as well as from previous work on the effect of forcing frequency on separated flows [12,13], we speculate that the forcing at frequencies higher than the natural shedding frequency of the separation bubble ($F^+ > 1$) may introduce effects that diminish the effectiveness of separation control. To investigate this further, an additional simulation has been performed with simple sinusoidal forcing at $F^+ = 2$, and the results are shown in Fig. 10. It is noted that, while the SIN jet at $F^+ = 1$ was quite effective, the forcing at $F^+ = 2$ is fairly ineffective and only reduces the separation bubble size to about 39δ. The topology of the vortex structures [Fig. 10(a)] shows that, although the vortices remain two-dimensional upstream of $x/\delta < 25$, they merge into a larger coherent vortex that breaks into smaller eddies further downstream. This behavior is similar to that observed for the BM case. The synthetic jet forcing at $F^+ = 2$ also makes the upstream shear layer ($x/\delta \sim 15$) lift up from the wall [see Fig. 10(b)] in a manner similar to the BM case. Note that the two-dimensional vortex roll-up of the upstream shear layer ($x/\delta < 20$) is not clearly observed in this case. This is due to the fact that the base flow shear layer instability is less susceptible to the frequency higher than its natural shedding frequency. These observations indicate that the high frequency forcing delays the vortex roll-up and promotes vortex paring and merging, both of which have negative effects on the reduction of the separation bubble size.

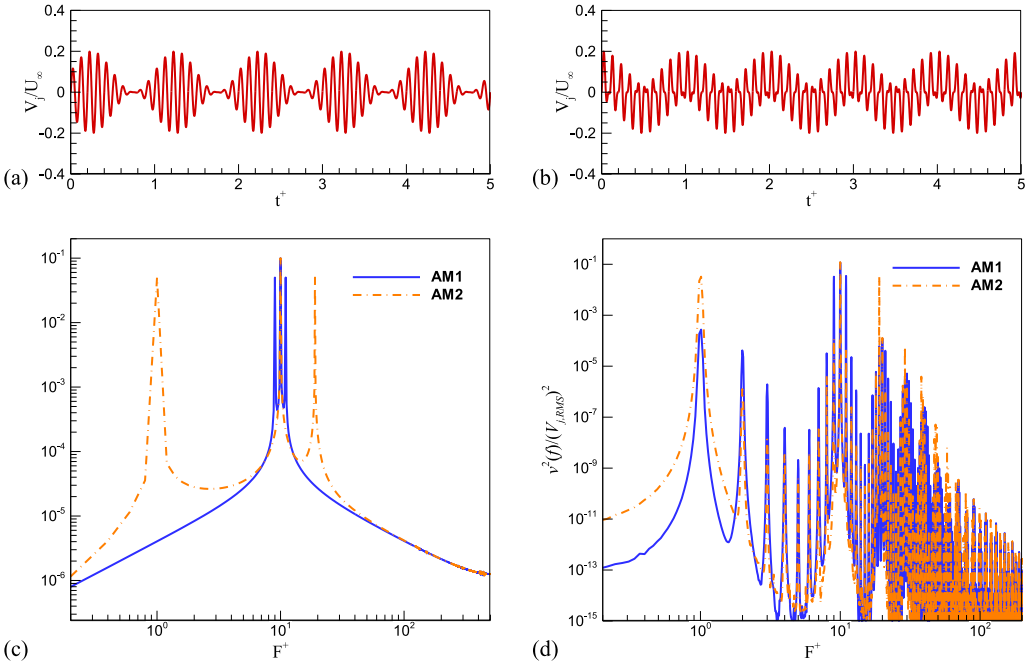

FIG. 11. (a) Waveform of synthetic jet velocity for AM1: amplitude modulation given by Eq. (4), $F_c^+ = 10$, $F_m^+ = 1$, and $t^+ = t f_0$. (b) waveform for AM2: tailored amplitude modulation scheme given by Eq. (9). (c) Spectra of the synthetic jet input velocities for AM1 and AM2. (d) Power spectra of vertical velocity monitored on the synthetic jet outlet port in the flow field.

E. Amplitude modulation schemes

The investigations in the previous sections suggest that the modulation scheme needs to be designed to produce the strongest possible forcing at the target frequency. The abrupt on-off control associated with burst modulation, however, results in imparting most of the energy to frequencies that are higher than the modulation frequency. Amplitude modulation (AM) is suggested as an alternative where the actuation amplitude is modulated smoothly by a sinusoidal function with a prescribed modulation frequency. The waveform of a widely used amplitude modulation [16,17] [Eq. (4)] is plotted in Fig. 11(a) for $F_c^+ = 10$ and $F_m^+ = 1$, and is referred to here as AM1. It is expected that the smooth adjustment of amplitude using a sinusoidal function at the modulation frequency will produce a more effective forcing at the targeted modulation frequency ($F_m^+ = 1$). The spectrum of the input signal for AM1 shown in Fig. 11(c) indicates, not surprisingly, that AM1 has discrete peaks at $F_c^+ - F_m^+, F_c^+$, and $F_c^+ + F_m^+$, but no peak at $F^+ = 1$. The AM1 jet produces spectral energy at $F^+ = 1$ primarily through nonlinear convection effects, but the normalized energy at $F^+ = 1$ for AM1 is about one order of magnitude smaller than that for the BM jet [see Fig. 11(d)] in the present simulation results. The current model does not include a finite height synthetic jet slot, which is known to generate additional nonlinear effects [23]. However, as shown in Appendix C, for the present flow conditions, the nonlinear effect is expected to be relatively small (<10% of the linear unsteady term) even for a more realistic actuator with a finite slot height and for more realistic external flow conditions. This suggests that, in general, AM1 may not be a very efficient modulation scheme for separation control, and this issue will be addressed later in this section.

In anticipation of this result, we also construct an alternate amplitude modulation scheme, which is prescribed as

$$V_{j,\mathrm{AM2}}(t) = \left(\frac{1}{2}\right) V_{\max} \sin(2\pi f_c t)[1 + \sin\{2\pi(f_c - f_m)t\}], \tag{9}$$

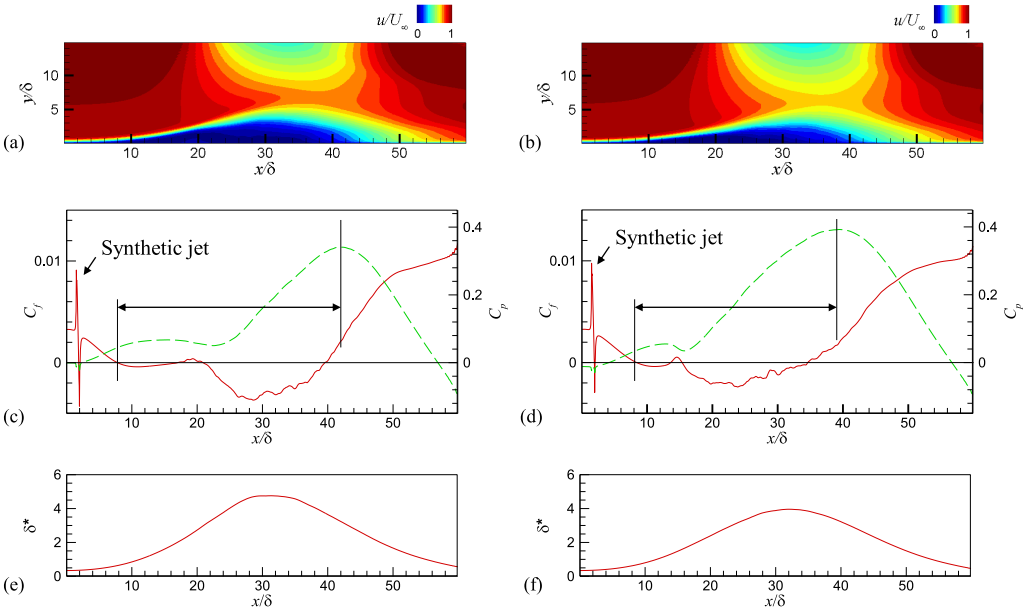

FIG. 12. Time averaged fields for the control cases with the amplitude modulated synthetic jet. Streamwise velocity contours for the AM1 jet (a) and AM2 jet (b) with $F_c^+ = 10$, $F_m^+ = 1$. Skin friction (solid line) and pressure (dashed line) coefficient profiles for AM1 (c) and AM2 (d). Mean displacement thickness along the streamwise direction for AM1 (e) and AM2 (f).

and is referred to here as AM2. The waveform and frequency spectrum for AM2 are plotted in Figs. 11(b) and 11(c) for $F_c^+ = 10$ and $F_m^+ = 1$, and it is clear from the plot that the AM2 signal has a strong and clear spectral peak at $F^+ = 1$, and no peaks at the higher harmonics of the modulation frequency. Note that the peak at $F^+ = 10$ is unavoidable since it is the main driving frequency ($F_c^+ = 10$). An additional peak at $2F_c^+ - F_m^+ (= 19)$ is also obtained. It is, however, expected that the separated bubble may not be receptive to this very high frequency and, furthermore, its effect should dissipate rapidly due to viscosity. The power spectrum of the synthetic jet velocity near the jet slot for AM2 is also plotted in Fig. 11(d), and the spectrum shows a noticeably dominant peak at $F^+ = 1$. The normalized energy at $F^+ = 1$ for AM2 is about two orders of magnitude higher than the one for the AM1, and also one order of magnitude higher than the BM. Overall, AM2 is expected to produce a stronger forcing at the desired modulation frequency ($F_m^+ = 1$).

Simulations are performed with both AM1 and AM2 synthetic jets, and the results are shown in Figs. 12 and 13. The parameters used for the AM1 and AM2 schemes are $F_m^+ = 1$, $F_c^+ = 10$, and $V_{\max} = 0.2U_\infty$, and the momentum coefficient C_μ is 0.0075 for both AM1 and AM2. The mean flow fields are shown in Figs. 12(a) and 12(b), and one can see that AM2 is indeed more effective for separation control than the AM1. For both cases, the separation point remains the same ($x/\delta = 8$), but the reattachment point for the AM2 moves slightly more upstream as compared to AM1. The mean separation bubble lengths are found to be about 34δ for the AM1 case and 31δ for the AM2 case, as shown in Figs. 12(c) and 12(d). The height of the separation bubble for AM2 is 3.95δ, and this is also noticeably smaller than that for AM1, which is 4.75δ [Figs. 12(e) and 12(f)]. It should be noted that the separation bubble for the AM1 actually has a greater height than for the BM jet case shown in Fig. 5(f).

The instantaneous flow fields presented in Fig. 13 show that the AM1 jet control case shares many flow features with the BM jet result. The two-dimensional vortex roll-up of the upstream shear layer ($x/\delta < 20$) is delayed and thus the shear layer is lifted from the wall in the upstream region [Fig. 13(a)]. Vortex pairing and merging as well as the resulting breakup of the coherent vortex

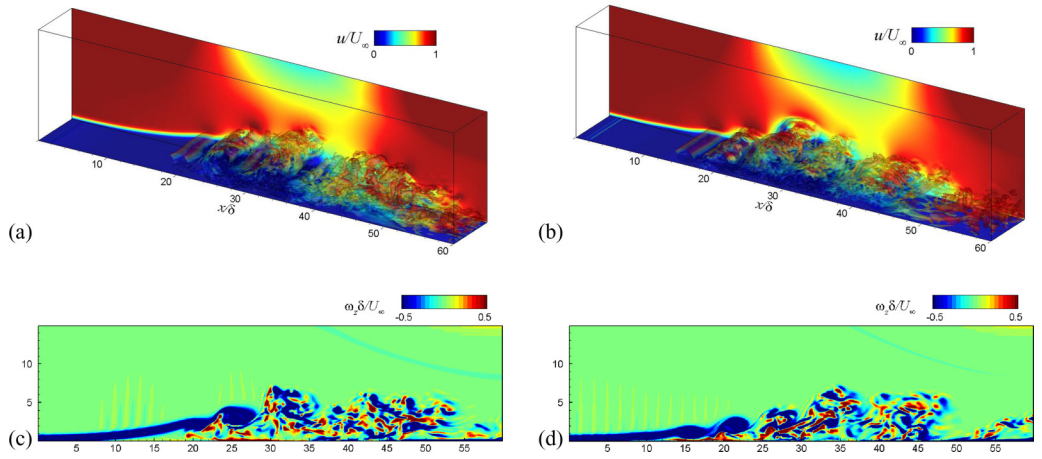

FIG. 13. Instantaneous flow fields for the control cases with the amplitude modulated synthetic jet. 3D vortical structure visualized by the isosurface of the second invariant of velocity gradients (Q_2) for the AM1 jet (a) and AM2 jet (b) with $F_c^+ = 10$, $F_m^+ = 1$. Spanwise vorticity (ω_z) contours for the AM1 jet (c) and AM2 jet (d).

into smaller eddies are also observed in the downstream [Figs. 13(a) and 13(c)]. For the AM2 jet case, the plot still shows the presence of vortex merging and large coherent structures [Figs. 13(b) and 13(d)]. However, the upstream shear layer remains close to the wall, and the initiation of the two-dimensional vortex roll-up of the upstream shear layer is clearly observed at around $x/\delta \sim 10$ [Fig. 13(d)]. This flow feature is very similar to that observed for the pure sinusoidal control case, and is likely connected to the fact that the forcing with the AM2 scheme imparts more energy at the modulation frequency than the AM1 and BM cases. As a result, the control with the AM2 jet is more effective in reducing the separation bubble size than the other modulation cases.

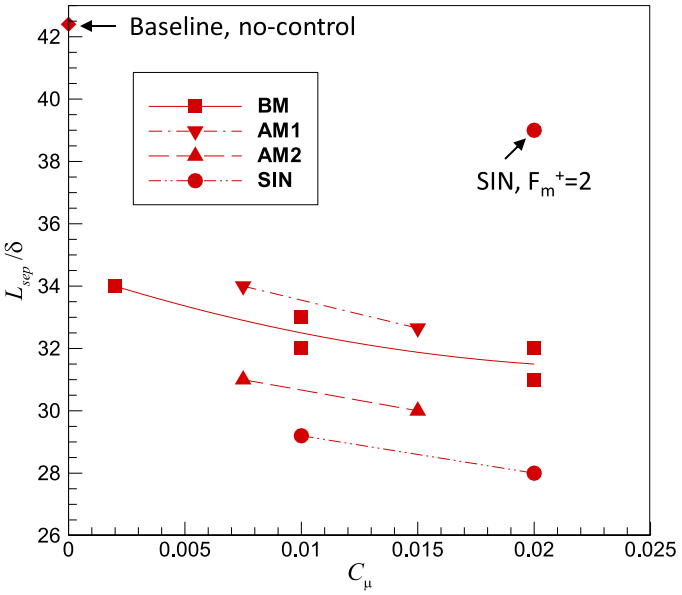

FIG. 14. Mean separation bubble length (L_{sep}) versus the momentum ratio coefficient (C_μ). The solid line represents the best quadratic fit for the BM cases. $F_m^+ = 1$ unless otherwise noted.

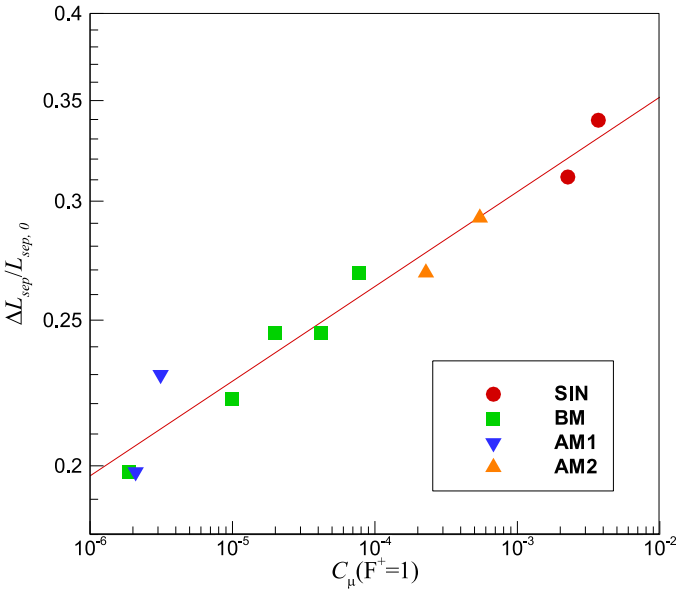

FIG. 15. Decrease of separation bubble length (ΔL_{sep}) normalized by the uncontrolled length ($L_{\text{sep},0}$) versus the spectral momentum ratio coefficient at $F^+ = 1$ [$C_\mu(F^+ = 1)$]. The solid line represents the best power-law fit.

F. Control effectiveness

In order to examine the trend of control effectiveness as a function of the momentum coefficient for both AM1 and AM2, additional simulations are performed for both cases with $C_\mu = 0.015$. The effect of synthetic jet modulation schemes on reducing the separation bubble length is then summarized in Fig. 14. The controlled mean separation bubble lengths are plotted as a function of the momentum coefficient C_μ. As discussed above, the SIN jet with the forcing at $F_m^+ = 1$ is the most effective in reducing the separation length. For the amplitude modulation schemes, the plot shows that the AM1 scheme is slightly less effective than the BM jet likely because the BM jet has more spectral energy at the target modulation frequency ($F^+ = 1$) than the AM1 jet. The plot also clearly indicates that the trend line for the AM2 jet lies between the BM and the SIN jets, and this reflects the greater effectiveness of this AM scheme. As pointed out above, this is because the controlled flow with the AM2 jet reproduces some of the key flow features observed in the pure sinusoidal forcing case. The AM2 jet, however, still includes high frequency forcing components, which inject effects that diminish control effectiveness, thereby making this control still less effective than the SIN jet.

It is also interesting to note that the effectiveness of separation bubble control by each modulation scheme summarized in Fig. 14 is correlated with the normalized spectral energy of the jet at $F^+ = 1$ produced by each scheme [see Figs. 9(b) and 11(d)]. The scheme with stronger energy at $F^+ = 1$ shows more effective separation bubble control (i.e., shorter separation bubble length). To examine this trend further, we define a spectral momentum coefficient,

$$C_\mu(f) = \frac{v^2(f)}{{U_\infty}^2}, \tag{10}$$

where $v^2(f)$ is the spectral energy of the jet velocity at the actuator outlet. According to our observation, the separation bubble control effectiveness (decrease of separation bubble length) should be positively correlated to the spectral momentum coefficient at $F^+ = 1$. In Fig. 15, the decrease of separation bubble length, $\Delta L_{\text{sep}} = L_{\text{sep},0} - L_{\text{sep}}$, where $L_{\text{sep},0}$ is the baseline separation length without control, is plotted versus $C_\mu(F^+ = 1)$ for all the synthetic jet control cases. The figure indeed

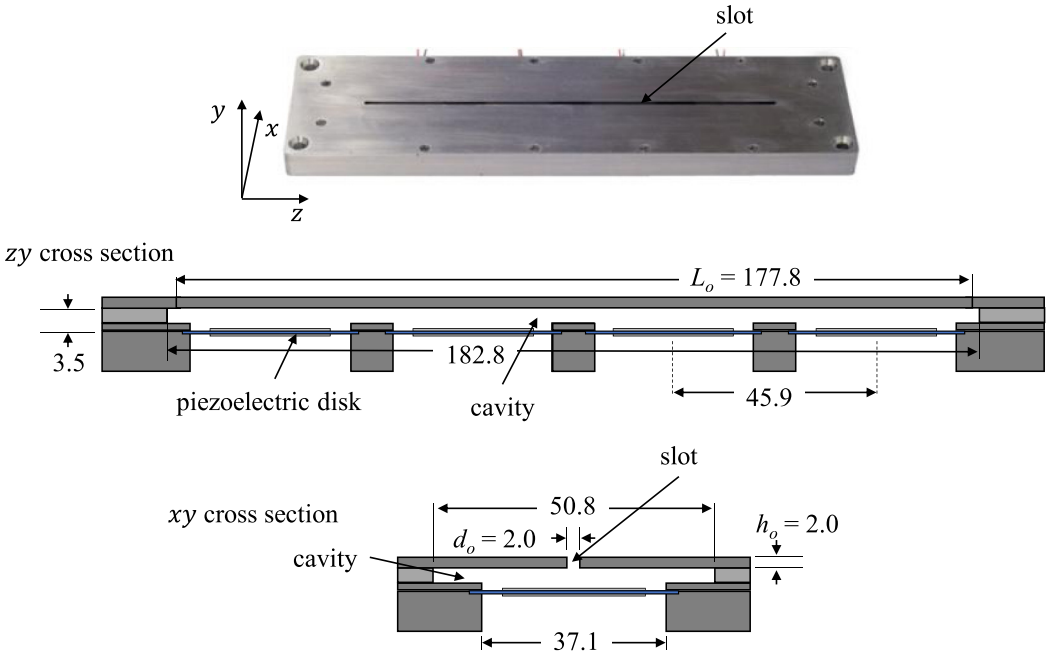

FIG. 16. Picture and schematic of the zero-net mass-flux actuator employed in the present study. All dimensions are in mm.

shows that the decrease in the size of the separation bubble is very well correlated with $C_\mu(F^+ = 1)$. In fact, the best-fit line for the current cases represents a power law:

$$\frac{\Delta L_{\text{sep}}}{L_{\text{sep},0}} = [C_\mu(F^+ = 1)]^\alpha, \tag{11}$$

with the exponent $\alpha = 0.063$ ($R^2 = 0.94$). This confirms that the separation bubble control effectiveness is strongly correlated to the synthetic jet energy at the target frequency corresponding to $F^+ = 1$. Effective modulation scheme can therefore be designed to maximize the energy of the jet at the target modulation frequency.

G. Experimental measurement of actuator output

In this final section of the paper, we demonstrate that the modulation scheme proposed here can in fact be realized with available synthetic jet actuators. So far in this paper, the proposed modulation schemes have been assessed via computational modeling, which does not account for the dependence of the actuator response to the modulation scheme. In reality, the output from an actuator may differ significantly from the input to the driver due to the resonance characteristics of the actuator as well as other flow-physics induced effects in the cavity and the slot of the actuator [24–26]. Thus, it remains to be shown that the spectral content of the jet output can preserve the characteristics of the input prescribed to the driver of an actuator, especially for the schemes examined here

For the current demonstration, we employ a zero-net mass-flux (ZNMF) actuator (see Fig. 16) comprising four piezoelectric disks (APC Inc., PZT5J, Part Number P412013T-JB) that serve to vary the volume of the cavity as unsteady voltages are applied across the disks. The actuator has a large-aspect-ratio rectangular slot of size $2 \times 2 \times 170$ (mm) and the slot exit is flush with a flat plate. In order to examine the effect of actuator efficiency, the energy spectra of the output jet velocities from the actuator are experimentally measured for three modulation schemes: BM with DC = 50%, AM1, and AM2. The actuator driving frequency is fixed at 2050 Hz, which is close to

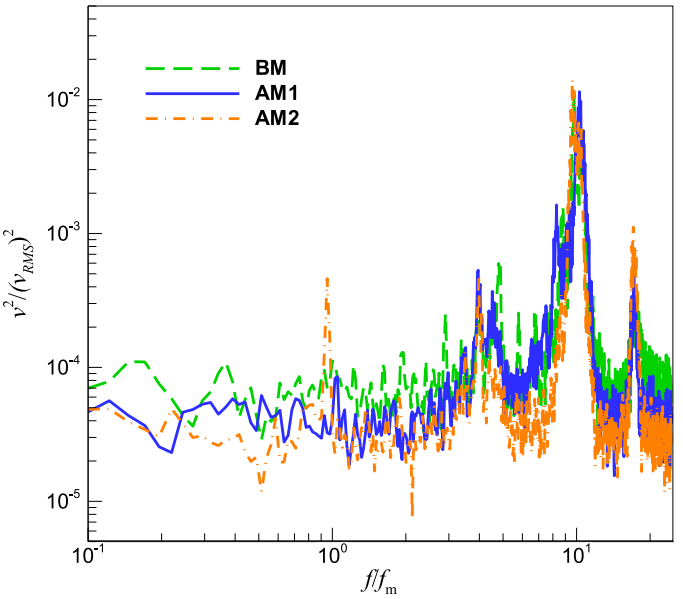

FIG. 17. Normalized energy spectra of the output jet velocities from the actuator measured in the experiments for the various input energy modulation schemes; BM: burst modulation [Eq. (3)] with DC = 50%; AM1: amplitude modulation by Eq. (4); and AM2: amplitude modulation by Eq. (9). The modulation frequency is f_m and the actuator driving frequency is $f_c = 10 f_m$.

the resonance frequency of the actuator. More details regarding the experimental model and actuator can be found in Ref. [27]. The modulation and driving frequencies are set to $f_m = 205$ Hz and $f_c = 2050$ Hz ($f_c/f_m = 10$) for all three modulation schemes corresponding to the condition used in the simulations ($F_c^+ = 10$). It should be noted that sinusoidal excitation at f_m generates negligible output by the current ZNMF actuator, thereby necessitating the use of a modulation scheme. The output jet velocity is measured at a distance of 0.177 mm from the slot exit.

The energy spectra of the output jet velocities for three modulation schemes are plotted in Fig. 17. The figure shows that the energy at the modulation frequency (f_m) is noticeably lower than the energy at the actuator driving frequency ($f_c = 10 f_m$) for the current setting. Nevertheless, the output for the AM2 modulation scheme clearly has more energy at f_m than for BM and AM1 (about 4 times and 6 times more energy than BM and AM1, respectively), and this is qualitatively in line with our computational models [Figs. 9(b) and 11(d)]. Thus, it is encouraging to note that despite the complex "transfer function" of such actuators, careful design of the modulation scheme can still be used to enhance the output energy at the target frequency. It remains to be shown that this increased energy input at the target frequency can be translated to better control authority in experiments.

IV. SUMMARY

The effect of synthetic jet modulation schemes on a laminar separation bubble has been investigated via direct numerical simulations. Simple, sinusoidal forcing with $F^+ = 1$ is considered as a reference case, and burst modulation with various parameters as well as amplitude modulation schemes are employed in the simulations. The simulations show that the burst modulation is always less effective than the simple sinusoidal forcing because of the altered flow characteristics. With burst modulation, the roll-up of the upstream shear layer into the vortices is delayed and high-frequency fluctuations inherent in burst modulation promote vortex pairing and merging, which diminishes control effectiveness. In contrast, sinusoidal forcing creates well-defined disturbances that remain coherent and two-dimensional over a longer distance, beyond which the flow transitions

to turbulence with no evidence of vortex merging. The commonly used amplitude modulation scheme produces the spectral peak at the modulation frequency through the nonlinear effect, while the input signal itself has no spectral peak at the modulation frequency. It is found that, however, the spectral energy at the modulation frequency for this scheme is relatively weak, and the scheme is slightly less effective than the burst modulation in terms of separation reduction. A modified amplitude modulation scheme that imparts significantly more energy at the requisite modulation frequency is found to be more effective than burst or conventional amplitude modulation schemes. Experiments with a piezoelectrically driven zero-net mass-flux actuator confirm that modulation schemes prescribed to the driver of the actuator can be preserved through the actuator and used to enhance the energy content at the target modulation frequency.

Although the practical aspects of the tailored amplitude modulation scheme need to be tested further in experiments, the present study suggests that the effectiveness of synthetic jet-based separation control could be improved by carefully designing the spectral content of the modulation scheme. A better understanding of the actuator efficiency for various modulation schemes and the scaling of nonlinear effects inside the actuator cavity, as well as the slot and the external flow, could be employed to develop new design tools as well as actuation schemes for flow control actuators.

ACKNOWLEDGMENT

This research is supported by AFOSR Grants No. FA9550-14-1-0289 and No. FA9550-17-1-0084 monitored by Dr. Douglas Smith.

APPENDIX A: GRID REFINEMENT STUDY

A grid refinement study is performed by employing coarser (384 × 96 × 32) and finer (768 × 256 × 32) resolution grids in addition to the baseline (512 × 128 × 32) resolution. The contours of the time and spanwise averaged, streamwise velocity are plotted in Fig. 18 for the results with

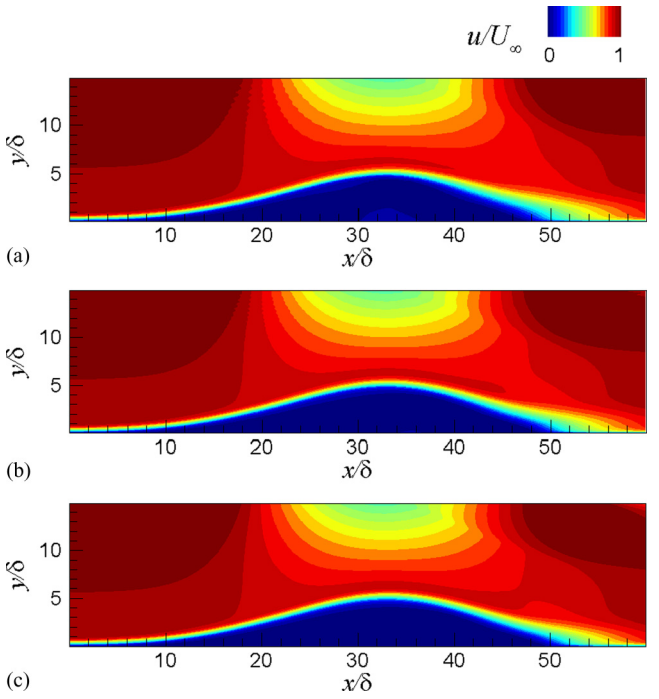

FIG. 18. Time and spanwise averaged, streamwise velocity contours with different grid resolutions. (a) coarse (384 × 96 × 32), (b) medium (512 × 128 × 32), and (c) fine (768 × 256 × 32) resolutions.

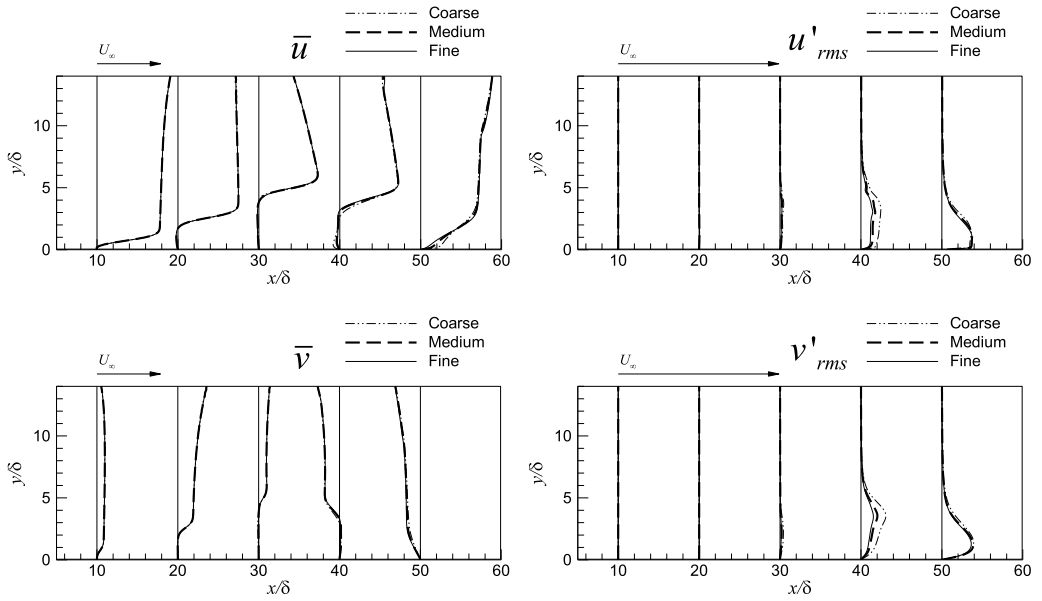

FIG. 19. Comparisons of the time and spanwise averaged $(\bar{u},\bar{v})$ and root-mean-squared fluctuation $(u'_{\rm rms},v'_{\rm rms})$ velocity profiles extracted at a number of streamwise locations for the different grid resolutions. The arrow indicates the scale of the inflow freestream velocity.

three different grid resolutions, and it is shown that the resolved separated flow is almost identical on the all three grids. For a quantitative comparison, velocity profiles are extracted for the time and spanwise averaged and root-mean-squared (RMS) fluctuations at a number of streamwise locations, and are presented in Fig. 19. The average velocity profiles on three different grids are found to be in reasonable agreement. The RMS fluctuation profiles also show good agreement. The maximum deviations between the computational grids occurs at $x/\delta = 40$, but even at this location the maximum differences in the RMS velocity fluctuations between the fine and medium grids is 2.5% of U_∞. Based on this, the medium resolution grid is considered adequate and employed for all the subsequent simulations.

APPENDIX B: ASSESSMENT OF SPANWISE RESOLUTION AND DOMAIN SIZE

For the assessment of spanwise resolution and domain size, we begin by examining the spanwise correlation of the computed flow for the baseline case (spanwise domain size is $L_z = 8\delta$ and the number of grid points in the spanwise direction is $N_z = 32$). As shown in Fig. 3(a), the flow is two-dimensional in the upstream region, and three-dimensional flow is mostly observed near and downstream of the reattachment point. Thus, the cross correlation coefficients for the spanwise distance (Δz) are calculated at these downstream locations by

$$C_{ab}(\Delta z) = \frac{\overline{a(z)b(z+\Delta z)}}{\sqrt{\overline{a^2(z)}}\sqrt{\overline{b^2(z+\Delta z)}}}, \tag{B1}$$

where the bar denotes temporal and spanwise average. The correlation coefficients at $y = 1.5\delta$ for the streamwise (u') and vertical (v') velocity fluctuations are plotted in Fig. 20. The plot shows that the correlation coefficients of the velocity fluctuations drop to magnitudes of 0.2 or lower within a spanwise distance of 4δ at the downstream locations $(x > 45\delta)$. This suggests that the spanwise domain size of $L_z = 8\delta$ is adequate to correctly model the spanwise structures in the flow. However, a significant drop in the spanwise correlation is not definitive proof of the adequacy of the spanwise

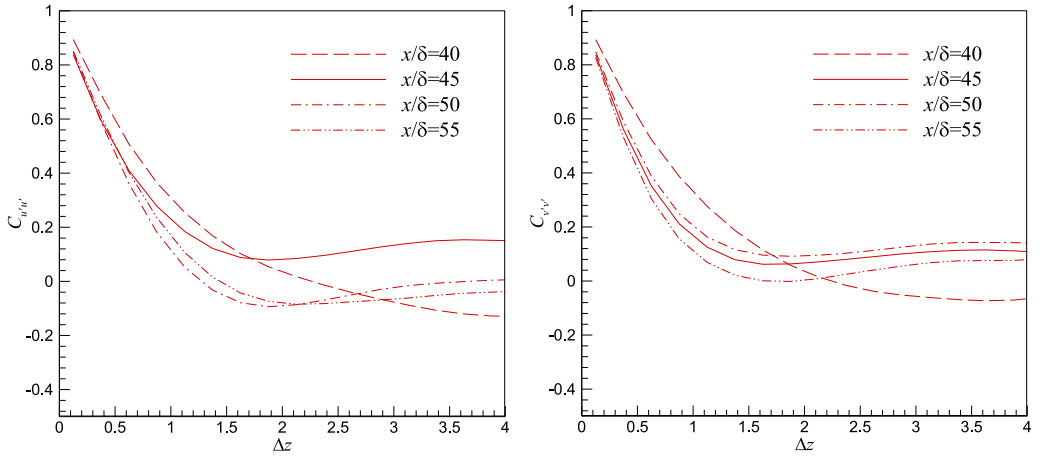

FIG. 20. Spanwise correlation coefficients for the streamwise ($C_{u'u'}$) and vertical ($C_{v'v'}$) velocity fluctuations at $y/\delta = 1.5$ and various streamwise locations for the baseline case with $L_z = 8\delta$ and $N_z = 32$ (L_z: spanwise domain size; N_z: number of grid points in the spanwise direction).

domain size. For this, we turn to a spanwise domain and resolution dependency study. In this study, simulations are performed with twice the spanwise resolution ($N_z = 64$) and twice the spanwise domain size ($L_z = 16\delta$). The average and RMS fluctuation velocity profiles are then compared at a number of streamwise locations in Fig. 21, and it is found that the results are almost identical for the spanwise resolutions and domain sizes considered. Thus, the behavior of the spanwise correlation and the domain dependency study together provide high confidence that a spanwise domain size of 8δ with 32 grid points is sufficient to accurately model this flow.

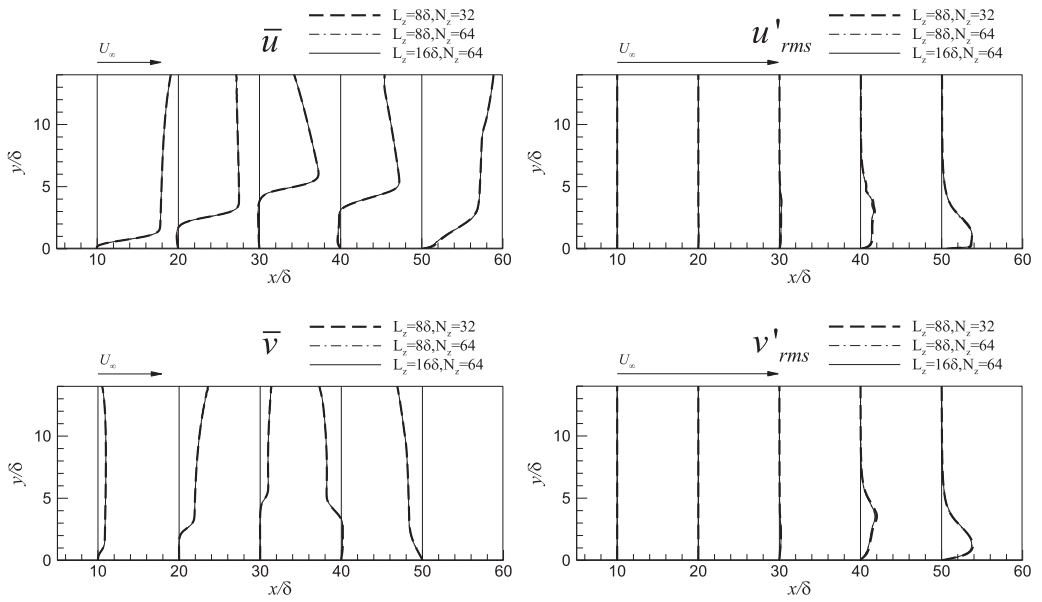

FIG. 21. Comparisons of the time and spanwise averaged ($\bar{u}, \bar{v}$) and root-mean-squared fluctuation ($u'_{\text{rms}}, v'_{\text{rms}}$) velocity profiles extracted at a number of streamwise locations for the different spanwise domain sizes and resolutions. The arrow indicates the scale of the inflow freestream velocity. L_z: spanwise domain size; N_z: number of grid points in the spanwise direction.

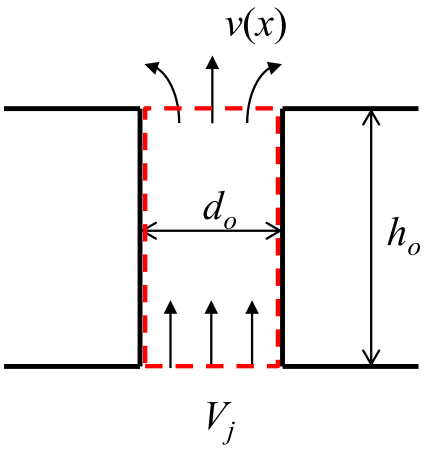

FIG. 22. A schematic of the synthetic jet outlet slot. The dashed box indicates the control volume for the analysis of pressure drop through the slot.

APPENDIX C: NONLINEAR EFFECTS IN SYNTHETIC JET FORCING

In the momentum forcing by a zero-net mass-flux (ZNMF) synthetic jet, the nonlinear effect associated with the pressure drop by jet expansion can introduce additional frequency components. In the previous work of Raju *et al.* [23], the nonlinear pressure drop is analyzed for the slot of the synthetic jet outlet nozzle. A schematic is shown in Fig. 22. For the incompressible flow, the pressure drop through the slot, Δp, can be expressed by the momentum balance for the control volume shown in Fig. 22:

$$\Delta p = \rho h_o \frac{\partial V_j}{\partial t} + \frac{1}{d_o}\int_0^{h_o} \tau_w dy + \frac{\rho}{d_o}\int_{-d_o/2}^{d_o/2} \left(v(x)^2 - {V_j}^2\right) dx, \tag{C1}$$

where h_o and d_o are the slot height and width, and τ_w is the wall shear stress on the slot wall. It is assumed that the inflow to the slot is a uniform plug flow with the input signal $V_j(t)$. The first term on the right-hand side of Eq. (C1) is a linear unsteady effect term directly associated with the inflow signal and, for a sinusoidal forcing with the amplitude $V_{\max}$ and frequency f, this term can be written as

$$\rho h_o \frac{\partial V_j}{\partial t} = \rho h_0 2\pi f V_{\max} \cos(2\pi f t). \tag{C2}$$

The last term in Eq. (C1) is the minor loss associated with flow development through the slot, and this term can generate additional frequency components via the action of the nonlinearity. The nonlinear minor loss term can be written with a nonlinear loss coefficient, K_d, as

$$\frac{\rho}{d_o}\int_{-d_o/2}^{d_o/2} \left(v(x)^2 - {V_j}^2\right) dx = K_d \frac{1}{2}\rho {V_{\max}}^2. \tag{C3}$$

Thus, the ratio of the magnitudes of the nonlinear and unsteady terms is given by

$$\frac{K_d {V_{\max}}^2/2}{2\pi h_o f V_{\max}} = \frac{K_d}{4\pi}\frac{1}{\mathrm{St}_{d_o}}\frac{d_o}{h_o}, \tag{C4}$$

where $\mathrm{St}_{d_o} = f d_o / V_{\max}$ is the Strouhal number based on the slot width and the magnitude of the jet. In the study of Raju *et al.* [23], a phenomenological model is proposed for the estimation of the loss coefficient, where K_d is given by the function of Stokes number, $S^* = \sqrt{2\pi f {d_o}^2/\nu}$. For the present

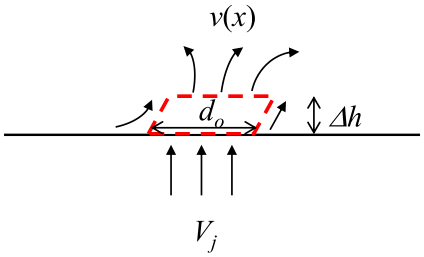

FIG. 23. A schematic for the control volume (dashed line) near the wall location where the synthetic jet is modeled as the velocity boundary condition. The control volume is taken along the local streamlines.

laminar separation bubble case ($\mathrm{Re}_\delta = 1000, V_{\max}/U_\infty = 0.2, d_o = 0.5\delta$), $\mathrm{St}_{d_o} = 0.15$, and $S^* = 9.7$ for $F^+ = 1$. For these parameter values, the model of Raju *et al.* [23] estimates K_d to be about 0.15 and the ratio in Eq. (C4) is about $0.08 d_o/h_o$. If the aspect ratio of the slot is $O(1)$, then the magnitude of the nonlinear effect term is estimated to be about 10% of the unsteady term. The ratio decreases for longer slots, as well as higher forcing frequencies and Reynolds numbers. Thus, for practical applications, where the Reynolds numbers and the target modulations frequencies are expected to be higher, the relative contribution of the nonlinear term is expected to be even smaller. The analysis therefore indicates that, in general, the contribution of the nonlinear term to the frequency content of the jet exit velocity is much smaller than that of the linear unsteady term.

In the present simulations, the slot of the synthetic jet nozzle is not considered and the synthetic jet is modeled by a sinusoidal velocity boundary condition at jet exit. Therefore, the additional nonlinear effect through the slot is not included in the simulations. The synthetic jet, however, still expands as it flows from the jet exit into the flow domain. By considering a small control volume near the wall location where the synthetic jet is modeled as shown in Fig. 23, it can be shown that the nonlinear effect associated with the expansion loss can be monitored in the flow field. The control volume is aligned with the local streamlines, and the pressure drop across the control volume in the vertical direction can be approximated as

$$\Delta p \approx \rho \Delta h \frac{\partial V_j}{\partial t} + \frac{\rho}{d_o} \int_{-d_o/2}^{d_o/2} \left(v(x)^2 - {V_j}^2 \right) dx, \tag{C5}$$

where Δh is the height of the control volume, and the viscous shear stresses are neglected. The first and second terms on the right-hand side of Eq. (C5) are the unsteady and nonlinear effect terms, respectively. The vertical velocity monitored in the flow field near the synthetic jet port should therefore contain the frequency components generated by the nonlinearity. Note, however, that the relative magnitude of the nonlinear effect could be different, and likely smaller, than that generated as the flow passes through the actuator slot.

[1] A. Glezer and M. Amitay, Synthetic jets, Annu. Rev. Fluid Mech. **34**, 503 (2002).
[2] A. Seifert, D. Greenblatt, and I. J. Wygnanski, Active separation control: An overview of Reynolds and Mach numbers effects, Aerosp. Sci. Technol. **8**, 569 (2004).
[3] A. Glezer, M. Amitay, and A. M. Honohan, Aspects of low- and high-frequency actuation for aerodynamic flow control, AIAA J. **43**, 1501, (2005).
[4] L. P. Melton, C. Yao, and A. Seifert, Active control of separation from the flap of a supercritical airfoil, AIAA J. **44**, 34 (2006).
[5] A. Glezer, Some aspects of aerodynamic flow control using synthetic-jet actuation, Philos. Trans. R. Soc. London A **369**, 1476 (2011).

[6] R. Mittal and P. Rampunggoon, On the virtual aeroshaping effect of synthetic jets, Phys. Fluids **14**, 1533 (2002).
[7] R. Mittal, R. Kotapati, and L. Cattafesta, Numerical study of resonant interactions and flow control in a canonical separated flow, in *43rd AIAA Aerospace Sciences Meeting and Exhibit* (AIAA, Reston, VA, 2005), p. 1261.
[8] D. P. Rizzetta and M. R. Visbal, Numerical simulation of separation control for transitional highly loaded low-pressure turbines, AIAA J. **43**, 1958 (2005).
[9] R. Duvigneau and M. Visonneau, Optimization of a synthetic jet actuator for aerodynamic stall control, Comput. Fluids **35**, 624 (2006).
[10] J. Dandois, E. Garnier, and P. Sagaut, Numerical simulation of active separation control by a synthetic jet, J. Fluid Mech. **574**, 25 (2007).
[11] D. You and P. Moin, Active control of flow separation over an airfoil using synthetic jets, J. Fluids Struct. **24**, 1349 (2008).
[12] R. Raju, R. Mittal, and L. Cattafesta, Dynamics of airfoil separation control using zero-net mass-flux forcing, AIAA J. **46**, 3103 (2008).
[13] R. B. Kotapati, R. Mittal, O. Marxen, F. Ham, D. You, and L. N. Cattafesta, Nonlinear dynamics and synthetic-jet-based control of a canonical separated flow, J. Fluid Mech. **654**, 65 (2010).
[14] M. A. Leschziner and S. Lardeau, Simulation of slot and round synthetic jets in the context of boundary-layer separation control, Philos. Trans. R. Soc. London A **369**, 1495 (2011).
[15] J. C. Griffin, M. Oyarzun, L. N. Cattafesta, J. H. Tu, and C. W. Rowley, Control of a canonical separated flow, in *43rd Fluid Dynamics Conference* (AIAA, Reston, VA, 2013), p. 2968.
[16] S. Margalit, D. Greenblatt, A. Seifert, and I. Wygnanski, Delta wing stall and roll control using segmented piezoelectric fluidic actuators, J. Aircraft **42**, 698 (2005).
[17] A. Qayoum, V. Gupta, P. K. Panigrahi, and K. Muralidhar, Influence of amplitude and frequency modulation on flow created by a synthetic jet actuator, Sens. Actuators A **162**, 36 (2010).
[18] E. A. Deem, L. N. Cattafesta, H. Zhang, C. W. Rowley, M. Hemati, F. Cadieux, and R. Mittal, Identifying dynamic modes of separated flow subject to ZNMF-based control from surface pressure measurements, in *47th AIAA Fluid Dynamics Conference* (AIAA, Reston, VA, 2017), p. 3309.
[19] E. Aram, R. Mittal, J. Griffin, and L. Cattafesta, Towards effective ZNMF jet based control of a canonical separated flow, in *5th Flow Control Conference* (AIAA, Reston, VA, 2010), p. 4705.
[20] R. Mittal, H. Dong, M. Bozkurttas, F. Najjar, A. Vargas, and A. von Loebbecke, A versatile sharp interface immersed boundary method for incompressible flows with complex boundaries, J. Comput. Phys. **227**, 4825 (2008).
[21] E. Adams and J. Johnston, Effects of the separating shear layer on the reattachment flow structure. Part 1: Pressure and turbulence quantities, Exp. Fluids **6**, 400 (1988).
[22] J. H. Seo, F. Cadieux, R. Mittal, E. A. Deem, and L. N. Cattafesta, Effect of synthetic jet modulation schemes on the response of a separation bubble, in *47th AIAA Fluid Dynamics Conference* (AIAA, Reston, VA, 2017), p. 3316.
[23] R. Raju, Q. Gallas, R. Mittal, and L. Cattafesta, Scaling of pressure drop for oscillatory flow through a slot, Phys. Fluids **19**, 078107 (2007).
[24] R. Raju, E. Aram, R. Mittal, and L. Cattafesta, Reduced-order models of zero-net mass-flux jets for large-scale flow control simulations, in *26th AIAA Applied Aerodynamics Conference* (AIAA, Reston, VA, 2008), p. 6404.
[25] L. N. Cattafesta III and M. Sheplak, Actuators for active flow control, Annu. Rev. Fluid Mech. **43**, 247 (2011).
[26] S. G. Sawant, M. Oyarzun, M. Sheplak, L. N. Cattafesta, and D. P. Arnold, Modeling of electrodynamic zero-net mass-flux actuators, AIAA J. **50**, 1347 (2012).
[27] E. A. Deem, L. N. Cattafesta, H. Yao, M. Hemati, H. Zhang, and C. W. Rowley, Experimental implementation of modal approaches for autonomous reattachment of separated flows, in *2018 AIAA Aerospace Sciences Meeting* (AIAA, Reston, VA, 2018), p. 1052.